Solar Energy Materials & Solar Cells 252 (2023) 112194

Contents lists available at ScienceDirect

Solar Energy Materials and Solar Cells

journal homepage: www.elsevier.com/locate/solmat

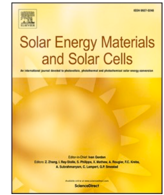

Zn/P ratio and microstructure defines carrier density and electrical transport mechanism in earth-abundant $Zn_{3-x}P_{2+y}$ thin films

Rajrupa Paul [a], Vanessa Conti [a], Mahdi Zamani [a], Simon Escobar-Steinvall [a,1], Héctor Sánchez-Martín [b], Carlotta Gastaldi [c], Mihai Adrian Ionescu [c], Ignacio Íñiquez-de-la-Torre [b], Mirjana Dimitrievska [a], Anna Fontcuberta i Morral [a,d], Valerio Piazza [a,*]

[a] Laboratory of Semiconductor Materials, Institute of Materials, School of Engineering, Ecole Polytechnique Fédérale de Lausanne, 1015, Lausanne, Switzerland
[b] Departmento de Física Aplicada and USAL-NANOLAB, Universidad de Salamanca, E-37008, Salamanca, Spain
[c] NanoLab, Institute of Electrical and Micro Engineering, School of Engineering, Ecole Polytechnique Fédérale de Lausanne, 1015, Lausanne, Switzerland
[d] Institute of Physics, School of Basic Sciences, Ecole Polytechnique Fédérale de Lausanne, 1015, Lausanne, Switzerland

ARTICLE INFO

Keywords:
Zn_3P_2 thin films
Electrical properties
Mobility
Earth-abundant semiconductors
Photovoltaics

ABSTRACT

Scalable and sustainable photovoltaic technologies require low-cost and earth-abundant semiconducting materials. Zinc phosphide is purported to be an absorber material with optimal photovoltaic properties. Herein we report the electrical properties of Zn_3P_2 thin films with different crystallinity grown on InP substrates. The room temperature electrical resistivity of the as-grown single crystal thin films is found to be in the range of 42–1050 Ω cm. We correlate the crystalline quality and composition to the electrical properties. Capacitance-voltage measurements and secondary ion mass spectroscopy demonstrate the direct correlation between the carrier concentration and the Zn/P ratio. The highest hole mobility value (125 cm^2/Vs) was obtained from high-quality single crystalline Zn_3P_2 thin films. The electrical characteristics of the heterojunction between the thin film and the substrate were also illustrated. This work sheds light on the electrical properties and conduction mechanism, thus providing a better understanding of the limitations and potentials of the electrical devices related to the material.

1. Introduction

A sustainable approach to large-scale deployment of photovoltaic technology must involve the utilization of earth-abundant solar cell materials. These materials can further reduce the cost associated with the terrestrial installation of solar cells, thus encouraging wide-scale deployment. Zinc phosphide (Zn_3P_2) is an earth-abundant photovoltaic absorber material with promising photovoltaic properties [1–4]. It exhibits a direct bandgap around 1.50 eV and a high absorption coefficient (10^4-10^5 cm^{-1}) in the visible light range near the band edge [5–11]. Additionally, it has a long minority carrier diffusion length (5–10 μm) and electrically passive grain boundaries [9,12]. All these characteristics are beneficial for its use in photovoltaic devices [13–16]. The highest reported efficiency for Zn_3P_2-based solar cells is approximately 6%, demonstrated for Mg/Zn_3P_2 Schottky junction solar cells by Bhushan and Catalano in 1981 [15]. A major limitation of Zn_3P_2-based solar cells is the lack of controllability on doping.

Zn_3P_2 is intrinsically p-type in nature due to the low formation energies of the Zn vacancies and P interstitials, which act as p-type dopants [17–21]. Previous studies have shown growth conditions play an integral role in the electrical properties of the samples [14,22,23]. Reported hole mobility values lie in the range of 10–300 cm^2/Vs at 300 K for Zn_3P_2 thin films [14,21–26]. Suda et al. reported a hole mobility value of 310 cm^2/Vs for epitaxial Zn_3P_2 thin films grown on GaAs (001) substrates [21]. In contrast, epitaxial thin films synthesized by Bosco et al. exhibited hole mobility values of 10–45 cm^2/Vs. For similar hole concentrations ($\sim 4 \times 10^{16}$ cm^{-3}) [14], the discrepancy in the hole mobility arises due to the difference in resistivity of the samples, which could be caused by the difference in the local microstructure and defect densities. These are largely dependent on the growth technique, growth condition,

* Corresponding author.
E-mail address: valerio.piazza@epfl.ch (V. Piazza).
[1] Current affiliation: Center for Analysis and Synthesis and NanoLund, Lund University, Box 124, 221 00 Lund, Sweden.

https://doi.org/10.1016/j.solmat.2023.112194
Received 29 September 2022; Received in revised form 30 December 2022; Accepted 9 January 2023
Available online 14 January 2023
0927-0248/© 2023 Published by Elsevier B.V.

and thermal history. A large variation has been observed in the room temperature resistivity of Zn_3P_2 thin films, resistivity values ranging from 0.1-10^6 Ω cm has been measured [16,22,27]. A systematic study on the effect of vapour composition during annealing showed the resistivity of the sample monotonically decreases with an increase in phosphorous partial pressure [22]. The corresponding Hall measurements showed an increase in the carrier concentrations (from 10^{12} to 10^{16} cm^{-3}) with no significant variation in mobility [22]. Thus, by regulating the composition of the vapour during growth or annealing, the p-type carrier concentration in Zn_3P_2 can be modified.

Doping the material n-type is challenging due to self-compensation by intrinsic acceptors. Studies indicate the introduction of the donor impurity is compensated by the formation of the intrinsic p-type defect in the crystal lattice [28,29]. Only a few instances of n-type doping of Zn_3P_2 have been reported. Suda et al. demonstrated the n-type doping of Zn_3P_2 thin films epitaxially grown on GaAs substrates [28]. Their results indicate that the presence of excess Zn during growth can lead to n-type doping of the material. The reported room-temperature electron mobility values were in the range 3000–7000 cm^2/Vs and the carrier concentration values were in the range of 3-9x10^{10} cm^{-3}. Furthermore, the measured carrier concentration did not increase above a certain point, instead, Zn segregation occurred. Additionally, the resistivity for the Zn_3P_2 epitaxial thin films was $\sim 10^3$–10^4 Ω cm, the low carrier concentration and high resistivity are attributed to the self-compensation effect of Zn_3P_2. Whereas, the electron mobility values reported by Katsube et al. for n-type doping of bulk Zn_3P_2 were <10 cm^2/Vs [29]. Low carrier concentration values were measured even though the bulk dopant concentration was about 10^{20} cm^{-3}.

Despite these previous attempts, Zn_3P_2 still lacks a reliable n-type doping route. Additionally, the literature is sparse for extrinsic p-type doping of Zn_3P_2. Even though there is a consensus about the intrinsic p-type nature of Zn_3P_2, there is a wide variation in mobility and resistivity values for similar types of materials. We believe that the limited efficiency of Zn_3P_2-based solar cells is largely due to the limited control of the electrical properties of the material, such as the minority carrier mobility and the carrier diffusion lengths. For a p-type absorber, the electrical behaviour of the minority carrier to a large extent determines the electrical performance of the solar cell. Furthermore, Stutz et al. recently highlighted the compositional tolerance of the Zn_3P_2 tetragonal unit cell. Compound compositions largely off-stoichiometric do not imply significant changes in the material phase or crystalline quality [30]. Still, variations in composition would impact the transport properties of the material and should be investigated.

In this work, we investigate the electrical properties of polycrystalline and monocrystalline Zn_3P_2 thin films grown on InP (100) substrates and correlate them to their chemical composition and microstructure. We demonstrate a device fabrication technique that circumvents challenges arising from micro-cracks present in monocrystalline thin films. We measure and compare the resistivity, carrier concentration, and mobility between polycrystalline and monocrystalline Zn_3P_2 thin films. Temperature-dependent measurements elucidated the defect states and their contribution to the transport in Zn_3P_2 thin films. We thus show that the growth conditions play a vital role in determining the electrical properties of the given thin films. Finally, we describe the junction behaviour between Zn_3P_2 and InP (n-, p-, and i-type), which gives an understanding of Zn_3P_2/InP-based devices. Our study provides an insight into the influence of composition on the electrical behaviour of Zn_3P_2 thin films, which in turn can help bridge the gap between the structural quality and functionality of Zn_3P_2 and provide the base to improve Zn_3P_2-based solar cell devices.

2. Materials and methods

2.1. Material growth and device fabrication

Zn_3P_2 thin films were grown on InP (100) substrates using a molecular beam epitaxy (Veeco GENxplor MBE) system equipped with separate zinc and phosphorous sources. Prior to the growth, the substrates were degassed in the MBE in three steps. In the first two steps, the substrate was degassed at 150 °C and 300 °C for 2 h, respectively. The third degassing step was carried out at 580°C under phosphorous beam equivalent pressure (BEP) > 1×10^{-6} Torr for 10 min (in the case of polycrystalline Zn_3P_2) and 30 min or longer (in the case of monocrystalline Zn_3P_2). During the growth, the manipulator temperature was set in the range of 240–270 °C. Additionally, the BEP of zinc and phosphorous fluxes were set to control the Zn/P ratio between 1.5 and 0.72. The detailed growth method is further explained in our previous paper [31].

Multiple electrical devices were fabricated on the samples to investigate the electrical properties of the as-grown monocrystalline Zn_3P_2 (mono-Zn_3P_2) and polycrystalline Zn_3P_2 (poly-Zn_3P_2) thin films with different techniques. The devices include structures for Hall Effect measurements, transmission line measurements (TLM), and capacitance-voltage (C–V) testing. Thin films grown on the undoped InP substrates allowed for the investigation of charge transport in Zn_3P_2. Whereas doped InP (both n-and p-type) and undoped (i-type) InP substrates were used to examine the current-voltage characteristic of Zn_3P_2/InP heterojunction.

Fig. 1a shows the schematic representation of the device fabrication steps. First, a 30 nm of Si_3N_4 layer is deposited on the Zn_3P_2 thin film using a plasma-enhanced chemical vapour deposition (PECVD) system. The samples underwent several electron beam lithographic (EBL) steps. The first EBL step defined the alignment markers, which are settled by metal (Cr/Au) sputtering. The second EBL step defined the device geometry: for this work, we chose a Hall bar geometry with varying dimensions (the lengths of the hall bars were in the range of 50–100 μm while keeping the geometrical proportions constant) to accommodate the micro-cracks forming in some of the mono-Zn_3P_2 samples due to the differential thermal expansion (as shown in Supplementary Fig. S1). Afterwards, reactive ion etching (RIE) was performed to remove the Si_3N_4 from the defined Hall bar structures. The final EBL step was performed to pattern the micro-contacts and subsequently, the metal contacts were deposited using sputtering. Au, Ag, or Pt allowed to obtain ohmic contacts, as these metals showed linear behaviour with Zn_3P_2 (as shown in Supplementary Fig. S2). Prior to any metal deposition, 30–45 s of Ar milling (at Ar flow of 50 sccm and 100 W power) was performed to remove the native oxide of the Zn_3P_2 to ensure good contact quality. As a final step, the devices were electrically isolated from the surrounding thin film using focused ion beam (FIB) milling. This approach allows to probe the charge transport via parallel and perpendicular paths in samples containing micro-cracks without the need for the correction factors required in the Van der Pauw approach for non-uniform continuous films [32]. For the sake of comparison, the same approach has been used for the poly-Zn_3P_2 sample although no micro-cracks were observed. Fig. 1b shows the SEM micrograph of the final device fabricated on the mono-Zn_3P_2 thin film. The processing of the structures for TLM and C–V measurements followed the same steps, except for the FIB milling. The C–V measurements were done in a planar configuration utilizing Schottky and ohmic contacts. Sputtered Al was used as the Schottky contact. The distance between the Schottky and the ohmic pads was varied from 1 to 1000 μm, to identify the parasitic effects arising from this configuration.

2.2. Measurement methods

The morphology of the thin films was characterized using a scanning electron microscope (Zeiss Merlin FE-SEM). The crystallinity and orientation were measured using out-of-plane diffraction on a Bruker D8 Discover Plus equipped with a Cu (K- α) rotating anode X-ray source (1.54 Å). Out-of-plane scans were performed using Dectris Eiger2 500 K detector in 2D scanning mode (gamma coverage of approximately 30°), and conditioning the primary beam with a focusing mirror and

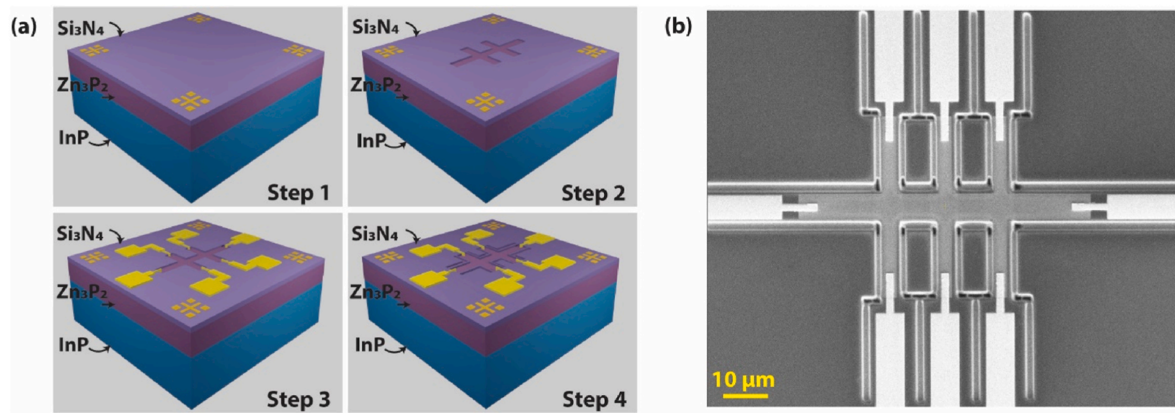

Fig. 1. Fabrication process of the electrical device on Zn_3P_2 thin films: (a) schematic representation of the device fabrication steps, (Step 1) alignment marker definition, (Step 2) Hall bar definition after the second EBL and RIE process, (Step 3) contact deposition using sputtering after the third EBL process, (Step 4) isolation of the device using FIB milling. (b) SEM image of the final device.

collimating optics of 0.5 mm. The Secondary Ion Mass Spectroscopy (SIMS) was carried out by Eurofins EAG laboratories. PHI Model 6600 Quadrupole Secondary Ion Mass Spectrometer was utilized to determine the concentration distribution of Zn_3P_2 and InP layers qualitatively, using ion implant standards with known concentrations for approximation. In quadrupole SIMS, Cs^+ is used as the primary beam and the molecular ions (CsE^+) of Cs and the ions of interest are counted in the quadrupole SIMS mass analyzer. The TLM and the current-voltage (I–V) measurements were done using a Keithley 6487 voltage source and picoammeter to apply voltage and measure the current. The voltage sweep range was between ±2 V. For 4-point measurements, a Keithley 6517A nanovoltmeter was used to measure the voltage. Temperature-dependent I–V measurements were done using a LakeShore CRX-VF cryogenic probe station, connected to a Keithley SCS 4200 used as ammeter and voltmeter. Four continuously variable temperature (ZN50R-CVT) probes allow the measurement of temperature sweeps without the need to lift and re-position the probes and the 336 controller adjusts the temperature. Hall Effect and temperature-dependent measurements were performed using a Physical Property Measurement System (PPMS® DynaCool™ by Quantum Design). The measurements can be carried out in a cryogenic temperature range (down to 2 K) and the built-in cryopump ensures high vacuum applications (<10^4 Torr). The excitation current was varied in the range of 0.1 μA–1 μA and the magnetic field was swept in the range ±5 T. All the C–V measurements have been performed at room temperature under ambient conditions using Keithley 4200A-SCS Parameter Analyzer with 4210-CVU module. The DC voltage was set in the range of ±2 V and the AC signal had a frequency of 1–2 MHz with a 30–50 mV amplitude.

3. Results and discussion

3.1. Structural properties of Zn_3P_2 thin films

We start by elucidating the structural differences between mono-

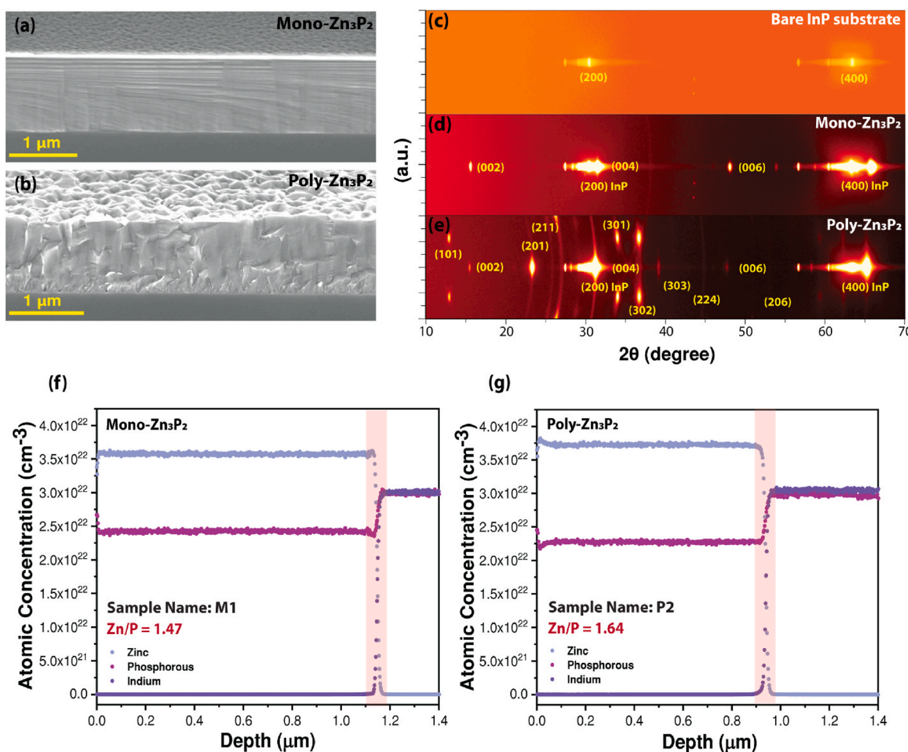

Fig. 2. Structural description of mono- and polycrystalline Zn_3P_2 thin films. Cross-sectional SEM micrographs of the (a) monocrystalline Zn_3P_2 thin film (b) polycrystalline Zn_3P_2 thin film. Out-of-plane diffraction patterns from: (c) InP (100) substrate; (d) monocrystalline Zn_3P_2 thin film showing only the {00h} family of planes; (e) polycrystalline Zn_3P_2 thin film showing a textured growth. SIMS measurements from: (f) monocrystalline Zn_3P_2 thin film (M1) with Zn/P ratio ~1.47; (g) polycrystalline Zn_3P_2 thin film (P2) with Zn/P ratio ~1.64.

Zn_3P_2 and poly-Zn_3P_2 thin films. Fig. 2a and b shows the representative SEM cross-section micrographs of the mono-Zn_3P_2 and poly-Zn_3P_2 thin film, respectively. The thickness of both thin films is ~1 μm. The cross-sectional morphology of the poly-Zn_3P_2 thin film is granulated and it has a columnar-like growth perpendicular to the substrate. The top surface of the poly-Zn_3P_2 thin film is distinctly rough, while the mono-Zn_3P_2 thin film has a smooth cross-sectional morphology and relatively flat top surface.

To identify the crystallographic growth direction and the relation with the substrate, out-of-plane scans were performed with an area detector using X-ray scattering. Fig. 2c show the resulting image of bare InP (100) substrate, where only the reflections associated with the (200) and (400) planes are observed. Fig. 2d and e shows the out-of-plane scans of mono-Zn_3P_2 and poly-Zn_3P_2 thin films, respectively. The reflections associated with the (002), (004), and (006) planes are observed for the mono-Zn_3P_2 thin film. Thus indicating the growth proceeds along the [001] direction and the epitaxial relation with the InP (100) substrate. Additionally, the intensity is concentrated in the spots, which is indicative of its highly ordered crystalline nature [33]. Whereas the poly-Zn_3P_2 thin film has textured growth, we observe a few different families of planes perpendicular to the growth direction. More prominent growth planes observed in X-ray scattering are (101), (201), and (200). We also investigate the compositional variation between the different crystalline thin films by SIMS which revealed a clear distinction in the composition of mono-Zn_3P_2 and poly-Zn_3P_2. The Zn/P ratio measured in the mono-Zn_3P_2 sample is ~1.47, which indicates the sample is slightly off-stoichiometric (as shown in Fig. 2f), with a small P excess. In contrast, the Zn/P ratio measured in the poly-Zn_3P_2 sample is ~1.64, indicating that the sample is Zn rich (as shown in Fig. 2g). For both samples, the interface between the thin film and the substrate is sharp and well-defined. It is important to note that we do observe a compositional variation among different samples. This variation is attributed to the growth conditions (such as temperature and flux), while the difference in crystallinity is mainly due to the degassing process [31]. In general, most of the poly-Zn_3P_2 thin films have a Zn/P ratio > 1.5. Whereas, the mono-Zn_3P_2 thin films have a Zn/P ratio ≤ 1.5. Table 1 contains an overview of the samples used in this study along with the characterization results obtained; hereon the sample name will be used to refer to a specific sample. It is worth-noting that the sample-to-sample compositional variation is due to the V/II ratio used for the epitaxial growth of the thin films.

3.2. *Resistivity measurements*

The characterization of the material's fundamental electrical properties in relation to their crystalline nature establishes the first step toward the realization of Zn_3P_2-based functional devices. Our investigation started from TLM measurements which enable us to describe the resistivity of the mono-Zn_3P_2 and poly-Zn_3P_2 thin films. Representative results obtained on different samples are outlined in Fig. 3, and resistivity values are reported in Table 1. Fig. 3a shows an optical microscope image of a typical device. It is constituted by a series of multiple electrical contacts with increasing distances ranging from 30 to 90 μm. The total resistance (R_{TOT}) between two metal contact pads is measured as a function of the distance between two contact pads. The equivalent circuit allows to describe the current-voltage relationship through a constant total resistance $R_{TOT} = 2R_M + 2R_C + R_S$, where R_M is the resistance of the metal, R_C is the contact resistance, and R_S is the resistance of the material between the electrical pads. As the R_M value is much smaller than the other terms, it can be neglected. Fig. 3b and c shows the TLM plots obtained from thin film samples M1 and P2 grown on i-InP substrates, respectively. The resistance increases linearly as a function of length, as expected. The contact resistance ($2R_C$) is obtained from the y-intercept of the plot of the linear fit. The estimated contact resistivity from the TLM plots is 0.95 ± 0.4 Ω cm^2 for M1 and 0.63 ± 0.05 kΩ cm^2 for P2. The contact resistivity value obtained from M1 is in the same range as previously reported values of as-deposited Au contacts on Zn_3P_2 [26]. It should be noted that we did not observe any significant reduction of the contact resistance when using other metals such as Ag, Pt, and Zn/Au. Thermal treatments are often used for reducing contact resistance. We did not apply any thermal treatment in this study as post-growth annealing could affect the thin film composition by desorption of Zn [11,34]. The resistivity values obtained from the poly-Zn_3P_2 (P1 and P2) thin films are in the range of 6500–9000 Ω cm, while the values obtained from the mono-Zn_3P_2 (M1 and M4) thin films are in the range of 150–1050 Ω cm. The vast difference in resistivity value can attributed to the presence of grain boundaries in the poly-Zn_3P_2 thin films, which could contribute to increased scattering of the charge carriers. The origin of the significant difference in resistivity will be clarified in Section 3.3.

Fig. 3d shows the TLM data obtained from M3, a mono-Zn_3P_2 thin film grown on n-type InP substrates, which demonstrates a distinctly different characteristic curve with respect to monocrystalline thin films grown on i-InP. Two distinct slopes can be observed from the plot, the first slope (depicted by the red dashed line) can be assigned to the Zn_3P_2 thin film. Whereas the second slope (depicted by the blue dashed line) is attributed to the flow of current into the substrate. A resistivity value of ~45 Ω cm and a contact resistivity value of 0.6 ± 0.17 Ω cm^2 are obtained by fitting the first slope of the TLM, in good agreement with the values obtained from the mono-Zn_3P_2 thin films grown on the i-InP substrate. These values support the hypothesis that the first slope of the TLM plot provides information regarding the thin film. The change in the TLM slope at a larger contact distance is accompanied by a change from linear to non-linear I–V curves (as shown in Supplementary Fig. S3). The change occurs when the distance between two contact pads increases to over 100 μm. We attribute the non-linearity of the I–V curves to the current crossing the heterojunction. In contrast, the I–V curves obtained from the (poly- and mono-) Zn_3P_2 on i-InP are linear irrespective of the distance between the two contact pads (as shown in Supplementary Fig. S2). The junction behaviour between the Zn_3P_2 and n-InP plays an integral role in the leakage current, where at critical distances over 100 μm the leakage current dominates. We will highlight this behaviour in Section 3.3 when describing the junction properties between Zn_3P_2 thin film and differently doped InP substrate. In light of these evidences, from here on, we discuss electric measurements on the thin films grown on i-InP, unless specified otherwise.

We now turn to the temperature dependence of the conductivity for different samples, to gain insight into the conduction mechanism in

Table 1
Sample list: for each sample, the name and corresponding substrate type are indicated together with the results on crystallinity, Zn/P ratio, resistivity, and carrier concentration found in this work.

Sample Name	Substrate type	Crystallinity	Zn/P	Resistivity (Ω.cm)	Carrier Concentration (cm^{-3})
M0	n-InP	Monocrystalline	1.164	51.6 ± 5.0	(1.22 ± 0.19) x10^{19}
M1	i-InP	Monocrystalline	1.469	154.6 ± 10.7	(4.03 ± 0 .31) x10^{15}
M2	n-InP	Monocrystalline	1.474	42.6 ± 9.8	(4.00 ± 0.23) x10^{15}
M3	n-InP	Monocrystalline	1.502	44.9 ± 3.7	(1.09 ± 0.11) x10^{15}
M4	i-InP	Monocrystalline	1.578	1050 ± 263	(1.17 ± 0.95) x10^{14}
P1	i-InP	Polycrystalline	1.610	8794 ± 350	(1.06 ± 0.15) x10^{13}
P2	i-InP	Polycrystalline	1.642	6632 ± 421	(3.84 ± 0.33) x10^{13}

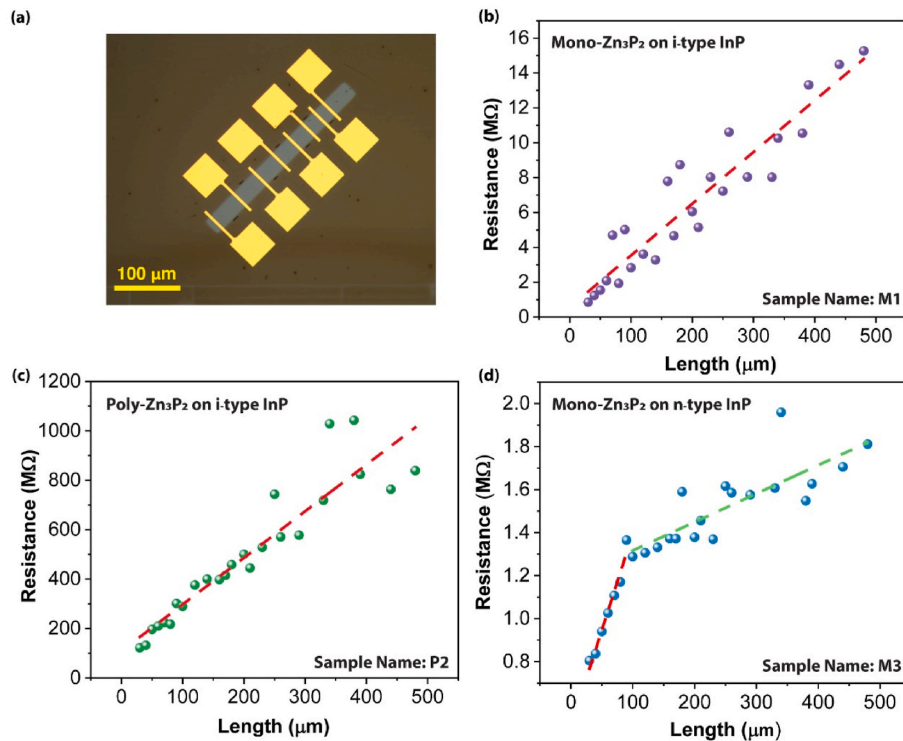

Fig. 3. TLM measurements: (a) Optical image of the TLM structure used for the measurements. TLM plots showing resistance as a function of the length, obtained from (a) monocrystalline Zn_3P_2 thin film (M1) (b) polycrystalline Zn_3P_2 thin film (P2), on i-InP (100) substrates (c) monocrystalline Zn_3P_2 thin film on n-InP (100) substrate (M3).

Zn_3P_2. Fig. 4a and b depict the dependence of resistivity with temperature for M1 and P2, respectively, over a range of 100–300 K. The resistivity of the thin films increases as the temperature decreases, in agreement with the semiconducting nature of the material. The increase in resistivity for P2 over a 200 K decrease in temperature is significantly steeper than the M1, suggesting a significant difference in charge transport in films with different crystalline texture. Thermally activated band conduction in semiconductors is described by an Arrhenius temperature dependence, given by Refs. [35,36]:

$$\sigma(T) = \sigma_0 e^{-\frac{E_a}{k_B T}} \tag{1}$$

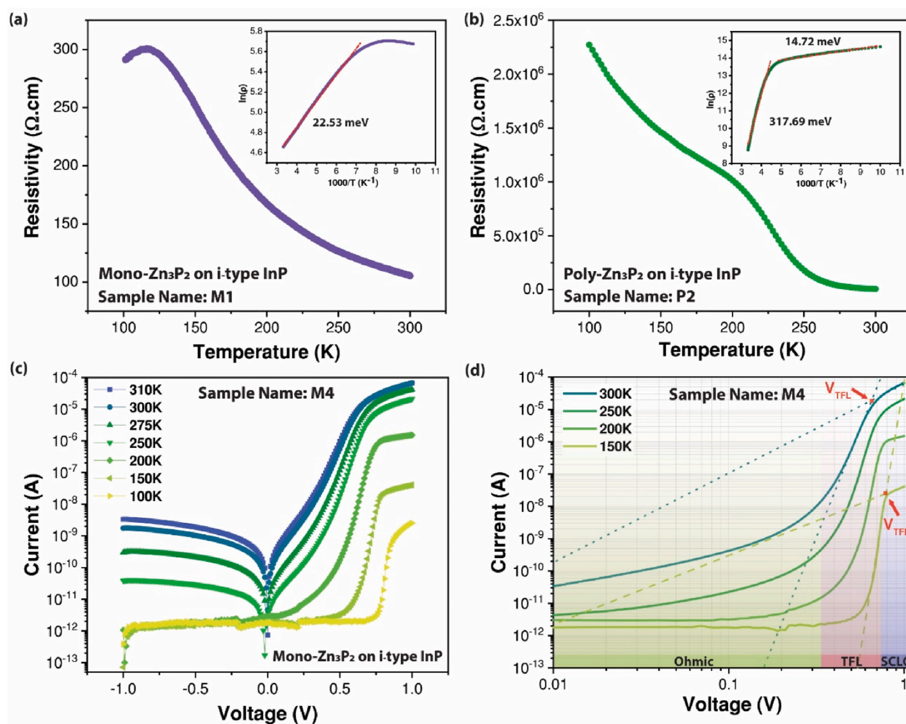

Fig. 4. Temperature-dependent resistance plot showcasing the semiconducting behaviour of different samples. (a) Monocrystalline Zn_3P_2 thin film (M1), and the corresponding fitting for thermally activated conduction (inset); (b) polycrystalline Zn_3P_2 thin film (P2), and the corresponding fitting for thermally activated conduction between 300 and 200 K and NNR between 200 and 100K (inset). (c) Temperature-dependent I–V characteristics obtained from monocrystalline Zn_3P_2 thin film with a Zn/P ratio ~1.58 (M4) plotted on a semi-logarithmic scale and (d) the corresponding temperature-dependent I–V characteristics plotted on a log-log scale where three distinct transport regions are visible: ($I \propto V$) Ohmic region, ($I \propto V^m$, $m > 2$) TFL region, and ($I \propto V^2$) SCLC region (the dashed lines represent the tangents with slopes 2 and 8 used for determining V_{TFL} at 300 K and slopes 2 and 15 for determining V_{TFL} at 150 K).

where σ_0 is a constant, E_a is the activation energy, and k_B is the Boltzmann constant. Given the exponential relation between thermally activated conduction and temperature, thermally activated band conduction is characterized by a linear relation in ln(σ) vs 1/T or ln(ρ) vs 1/T plots. The insets in Fig. 4a and b shows the corresponding plots of ln (ρ) vs 1/T which fit very good the expected linear behaviour for higher temperature values. For the temperature range of 150–300 K, the activation energy obtained for M1 is 22.53 meV. This value is consistent with the energy levels expected for phosphorus interstitial in bulk Zn_3P_2. It is worth to note that both phosphorous interstitials and zinc vacancies act as acceptors in Zn_3P_2, typically zinc vacancies have energy levels ranging from 190 meV to 290 meV and phosphorous interstitials have energy levels ranging from 14 meV to 90 meV [18,20,30,37]. For temperature values less than 150 K we observe a gradual decrease in resistivity, which can be attributed to the interplay of temperature variations of the carrier density and mobility. The carrier density diminishes with a decrease in temperature while the mobility increases, thus the resistivity has a minimum typically around 70 K [38].

The activation energy obtained from P2 was 317.69 meV for the temperature range of 200–300 K. This activation energy is slightly higher than the expected energy level for zinc vacancy levels [20]. The activation energy value could be due to the presence of crystalline disorder in the polycrystalline thin film. Still, one should note that the activation energy in the thermally activated conduction regime depends on the carrier concentration and the impurity energy levels [36]. A decrease in carrier concentration due to a lower amount of acceptors would lead to an increase in the activation energy due to the change in the Fermi level. Nonetheless, it is evident that the thermally activated conduction mechanism dominates at higher temperatures (above 200 K for P2 and above 150 K for M1) for both thin films. At temperatures below 200 K, a distinct change in the slope of the ln(ρ) vs 1/T plot is observed, indicating a change in the conduction mechanism. A hypothesis is that at lower temperatures, holes are recaptured by the acceptors and hopping starts to be the dominating mechanism. There are two types of hopping mechanisms that dominate the conduction process in semiconductors at lower temperature ranges, which are Nearest-Neighbour Hopping (NNH) and Variable Range Hopping (VRH) [35,36,39–41]. NNH and VRH can coexist in a material, however, NNH usually tends to dominate at higher temperatures. In NNH, the holes hop to the nearest-neighbour vacant site and this requires a thermal activation. The activation energy for NNH is much lower than that for thermally activated band conduction. For the NNH conduction, temperature and conductivity have a similar exponential dependence [35]. By fitting the temperature dependence of the resistivity in the range between 100 and 200 K, an activation energy value of 14.72 meV can be estimated. On further decreasing the temperature, the VRH conduction mechanism often comes into play. Here charge carriers hop between levels close to the Fermi level irrespective of their spatial distribution [42]. The plotted data (ln ρ vs 1/T) does not show any deviation from linearity in the measured range (200-100 K). Therefore we conclude, that for the measured temperature range, we do not observe the VRH (for which conductivity can be expressed as $\sigma = \sigma_0 e^{-[T_0/T]^{1/4}}$, where T_0 is the characteristic temperature, and σ_0 is a constant parameter) conduction mechanism as this would lead to a non-linear behaviour in the semi-logarithmic plot [39].

Now we turn toward a specific sample (M4) that showed atypical I–V characteristics. Fig. 4c shows the semi-logarithmic I–V plots measured at different temperatures for M4 (that has a high Zn/P ratio ~1.58). The typical I–V characteristic of mono-Zn_3P_2 and poly-Zn_3P_2 thin films are linear (as shown in Supplementary Fig. S2). The I–V plots obtained from sample M4 show a non-linear asymmetric behaviour and demonstrate a deviation from the ohmic or Schottky behaviour [38]. Furthermore, on decreasing the temperature, the overall current decreases and the deviation become more pronounced. To understand the electrical properties of the sample, the I–V characteristic in the forward bias is plotted in a log-log scale, as shown in Fig. 4d. The slope of the log-log plot gives the power dependence of current and voltage [43,44]. At low voltages (below 0.2 V) an ohmic relation is observed between the current and voltage ($I \propto V$) over all the measured temperature ranges. Between the voltage ranges of 0.2–0.7 V, the slope changes to 8 for 300 K and 15 for 150 K ($I \propto V^m$, where m is the slope in the log-log plot). Whereas above 0.7 V the slope is 2 ($I \propto V^2$) for all the temperature ranges. We observe three distinct regimes in the log-log I–V plot: first, a low-voltage ohmic regime with a slope of 1, followed by a trap filling regime with a large slope (>2), and a high voltage space-charge-limited current (SCLC) regime with a slope of 2. The SCLC conduction mechanism has been widely reported for organic semiconductors and insulators [45–48]. There are also some instances of SCLC conduction in inorganic semiconductors such as III-nitrides and semi-insulating II-V materials [49,50]. The presence of trapping states caused by impurities and defects can capture and immobilize a fraction of the injected carriers, thereby influencing the current transport process. Zn_3P_2 is known to form band tails due to the presence of impurity levels [30] and deep-level traps at ~0.7 eV [18,51]. Depending on the trap density and distribution, it might be feasible to observe SCLC conduction in Zn_3P_2. The trap density can be calculated from the trap-filled-limit voltage, given by Ref. [45]:

$$V_{tfl} = \frac{q n_t L^2}{2\varepsilon} \tag{2}$$

where q is the elementary charge, n_t is the trap density, L is the thickness, and ε is the dielectric constant. The crossing point between the tangent of the SCLC and the trap-filled-limited (TFL) regimes is used as the V_{tfl} [45]. By using Eq. (2), we obtained trap density values of 3.62×10^{13} cm^{-3} and 4.28×10^{13} cm^{-3} for 300 and 150 K, respectively. SCLC measurements are often used to extract the mobility of the carrier, where the mobility value is extracted from the quadratic regime. However, the estimation of mobility is prone to misinterpretation [45,52]. Given the asymmetric nature of the I–V plot, we decided not to use this method to extract the mobility values.

3.3. *Carrier density and heterojunction behaviour*

Hall Effect measurements can be used to measure the carrier density. However, our measurements showed a non-linear transverse resistance behaviour (refer to Supplementary Fig. S4 for more information). Therefore, we investigated the carrier concentrations in different thin films using C–V measurements. Fig. 5a shows the schematic representation of the planar configuration used for the measurements. The set-up consists of two adjacent dissimilar contacts, separated by a distance L_t. As for the previous measurements. Au is used as ohmic contact, while the Al is used as Schottky contact. Fig. 5b and c shows $1/C^2$ against voltage, also known as the Mott-Schottky plot, for M1 and P2 samples, respectively. The data display a negative Mott-Schottky slope, indicating a p-type conductivity for all the measured Zn_3P_2 thin films [53]. For a Schottky-diode under bias, the C–V relation can be expressed as [54]:

$$\frac{A^2}{C^2} = \frac{2\left(V_{bi} - V - \frac{kT}{q}\right)}{q \varepsilon s N} \tag{3}$$

where C is the capacitance, V_{bi} is the built-in potential of the diode, εs is the relative permittivity of Zn_3P_2, A is the area of the anode, and N is the carrier concentration. The slope of the Mott-Schottky plot gives the carrier concentration and the x-axis intercept gives the V_{bi}. The carrier concentration for M1 was found to be ~4.03×10^{15} cm^{-3}, whereas the carrier concentration of P2 was ~3.84×10^{13} cm^{-3}. We did not observe any significant variation in the carrier concentration by changing the distance (L_t) between the contact pads in the investigated contact distance range. While the carrier density difference between the monocrystalline and polycrystalline samples could eventually be attributed to the microstructure, one should also consider the chemical composition.

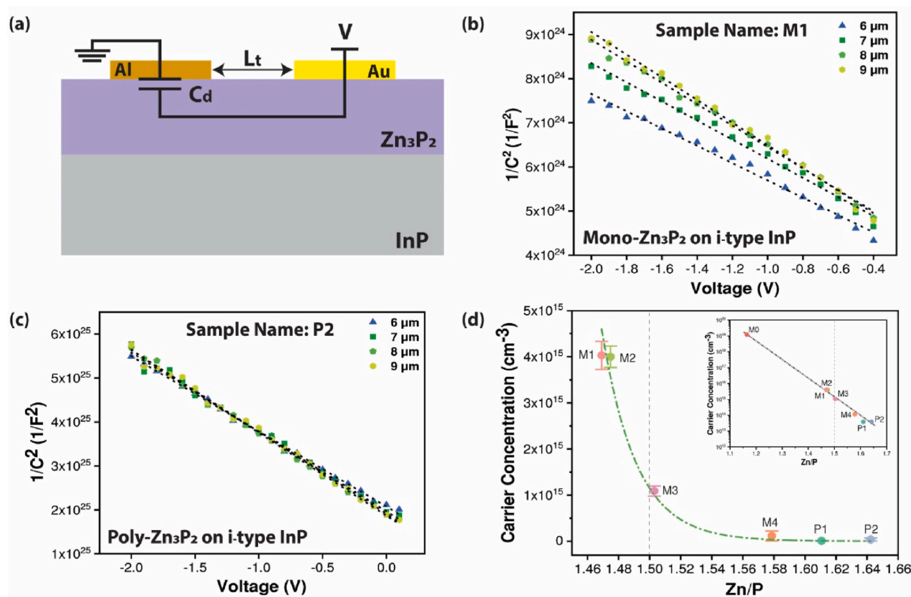

Fig. 5. C–V measurements and carrier density: (a) schematic representation of the planar configuration used for the C–V measurements, L_t is the distance between the Schottky and the ohmic contacts. The C–V plot obtained by varying L_t from (b) monocrystalline Zn_3P_2 thin film (M1) (c) polycrystalline Zn_3P_2 thin film (P2). (d) Plot showing the measured carrier concentration as a function of the Zn/P ratio (the error bars represent standard deviation due to L_t variation for each sample), the corresponding semi-logarithmic plot (inset) highlights the sample with the highest carrier concentration (1.22×10^{19} cm^{-3}) and lowest Zn/P (1.16) ratio. The stoichiometric Zn/P ratio is at 1.5, represented by the dashed line. The details of the plotted sample are listed in Table 1.

Zn_3P_2 is an unusual compound semiconductor as the Zn/P ratio can deviate strongly from 3/2 without loss of the semiconductor functionality [2]. The temperature dependence of the samples has also hinted at a relation between the composition and the carrier density, as given by the different activation energy for the relatively zinc richer or poorer nature of samples M1 and P2. These activation energies could be related to Zn vacancies and P interstitials, which act as dopants in the material.

To clarify the interplay between composition, microstructure and carrier density, we correlated the compositional analysis performed using SIMS with the carrier density obtained from the capacitance method (see Table 1). The results are presented in Fig. 5d. The carrier concentration ($\sim 1.22 \times 10^{19}$ cm^{-3}) is highest for M0 that has a Zn/P = 1.16. The carrier concentration strongly decreases for Zn/P ratios approaching 1.5. The sample M3 that is almost at stoichiometry (Zn/P =1.502) has a carrier concentration of $\sim 1.09 \times 10^{15}$ cm^{-3}. For Zn/P > 1.5 carrier densities are extremely low, below $\sim 1.5 \times 10^{14}$ cm^{-3}. The measured carrier concentrations as a function of the Zn/P ratio for different samples follow an exponential behaviour. To further confirm this, Fig. 5d inset depicts the data in a semi-logarithmic scale, which displays the linear behaviour and shows the sample with the highest carrier concentration in the same plot.

The role of chemical composition in carrier density can be found in the nature of interstitials in Zn_3P_2. P interstitials act as a p-type dopant with low formation energy in Zn_3P_2 [17,55], thus explaining the increased carrier concentration in the samples with Zn/P less than 1.5. Conversely, Zn inclusion in the lattice should act as an n-type dopant in Zn_3P_2 [55]. However, we do not observe n-type nature in any of the samples with a high Zn/P ratio. This is attributed to the prevalent self-compensation effect in Zn_3P_2 [29,56]. Given the low formation energy of P interstitials, excess Zn in the material is compensated by their formation. This results in a decrease in the carrier concentration with an increase in the Zn/P ratio. Additionally, this also leads to higher resistivity in the sample [22]. The monocrystalline Zn_3P_2 thin film with a higher Zn/P ratio (M4) exhibits higher resistivity ($\sim$1050 Ω cm) in comparison to the stoichiometric monocrystalline Zn_3P_2 thin film (M3) that has resistivity of $\sim$45 Ω cm. We extract the mobility values using $\sigma = nq\mu$, where σ is the conductivity obtained from TLM, while n is the carrier concentration obtained from C–V profiling. For monocrystalline samples, the mobility values are in the range of 15–125 cm^2/Vs, whereas for polycrystalline samples, the mobility values are in the range of 19–60 cm^2/Vs. The higher values of mobility obtained from the monocrystalline Zn_3P_2 thin films are among the upper bound of values reported in the literature for Zn_3P_2 [21,57], thus indicating the high-quality crystalline Zn_3P_2 thin films.

Finally, we probe the junction behaviour between the Zn_3P_2 thin film and the InP substrate. Fig. 6a inset shows the configuration used for the J-V measurements. Fig. 6a shows the comparison of the J-V characteristics of mono-Zn_3P_2 and poly-Zn_3P_2 thin films grown on i-InP substrate. Both thin films exhibit a rectifying behaviour. The current density values obtained at higher voltages from mono-Zn_3P_2 are much higher in comparison to the poly-Zn_3P_2. We attribute the lower current density value of the polycrystalline thin film to the high resistivity in the material. To better understand the influence of the doping in the InP on the junction behaviour we measure the J-V characteristic of Zn_3P_2 thin films grown on differently doped InP substrates. Fig. 6b shows the semi-logarithmic plot of the J-V characteristic obtained from monocrystalline Zn_3P_2 thin films grown on (p-, n-, i-) InP and polycrystalline Zn_3P_2 grown on i-InP. The Zn_3P_2 thin film grown on p-InP illustrates a linear and symmetric behaviour, which is indicative of a poor diodic behaviour between the two p-type materials (theoretical band alignment between p-type Zn_3P_2 and p-type InP is shown in Supplementary Fig. S5). When comparing the J-V characteristic of monocrystalline Zn_3P_2 on i-InP and n-InP we observe in the case of n-InP there is a large leakage current in the reverse bias. Additionally, the thin film grown on i-InP has a much greater threshold voltage value (0.68 V) in comparison to the thin film grown on n-InP (0.47 V). Moreover, the ideality factor obtained on fitting the linear part of the J-V plot was 2.03 ± 0.14 for thin film grown on i-InP and 3.46 ± 0.2 for thin film grown on n-InP. These differences demonstrate the monocrystalline Zn_3P_2 thin film grown in i-InP has relatively better diode parameters than the ones on n-InP. Thus, the junction behaviour between monocrystalline Zn_3P_2 and n-InP corroborates the flow of current into the substrate during TLM measurements.

4. Conclusion

In conclusion, we compared and contrasted the difference in the structural, compositional, and electrical behaviour between polycrystalline Zn_3P_2 and monocrystalline Zn_3P_2 thin films. We identified the conduction mechanism involved in different crystalline Zn_3P_2 thin films. Thermally activated conduction mechanism dominates at higher temperatures, whereas nearest-neighbour hopping mechanism was observed for polycrystalline thin films at lower temperatures. The corresponding activation energies obtained from our measurements are primarily associated with the P interstitials and Zn vacancies.

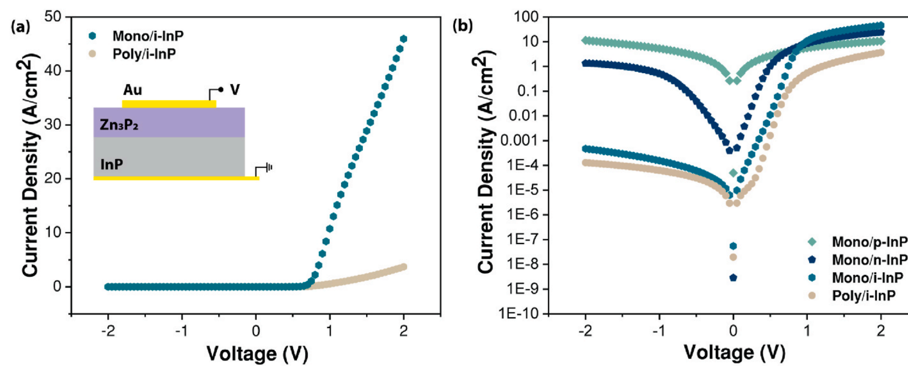

Fig. 6. Zn_3P_2/InP heterojuction behaviour: (a) J-V characteristic of the monocrystalline and polycrystalline Zn_3P_2 thin film grown on i-InP (100) substrate measured in a top-down configuration (inset). (b) Semi-logarithmic J-V curve obtained from monocrystalline Zn_3P_2 thin film grown on (p-, n-, i-) InP substrates and polycrystalline Zn_3P_2 thin film grown on i-InP.

Temperature-dependent I–V characteristic of Zn_3P_2 thin film with low carrier concentration revealed the occurrence of SCLC transport. High-quality monocrystalline Zn_3P_2 thin films with moderate carrier concertation demonstrated a high hole mobility (125 cm^2/Vs) at room temperature, indicating the growth conditions and composition of the material play an integral role in tuning the material functionality. We unveiled the impact of unintentional doping caused due changes in the Zn/P ratio on the electrical properties of the material. Carrier concentrations were directly correlated to the Zn/P ratio. They were attributed to a variation in Zn vacancies and P interstitials, in agreement with the activation energies deduced for conductivity. Finally, the effect of substrate doping on the electrical behaviour of the heterojunction has been highlighted. Hence, the present study provides insight into the electrical properties of Zn_3P_2 thin films and allows for a better understanding of the limitations and prospects of Zn_3P_2 thin film-based solar cells.

CRediT authorship contribution statement

Rajrupa Paul: Writing – original draft, Methodology, Investigation, Formal analysis, Data curation, Conceptualization. **Vanessa Conti:** Methodology, Data curation. **Mahdi Zamani:** Methodology. **Simon Escobar-Steinvall:** Writing – review & editing, Methodology. **Héctor Sánchez-Martín:** Methodology. **Carlotta Gastaldi:** Methodology. **Mihai Adrian Ionescu:** Resources. **Ignacio Íñiquez-de-la-Torre:** Resources. **Mirjana Dimitrievska:** Writing – review & editing, Supervision, Conceptualization. **Anna Fontcuberta i Morral:** Writing – review & editing, Validation, Supervision, Resources, Conceptualization. **Valerio Piazza:** Writing – review & editing, Validation, Supervision, Conceptualization.

Declaration of competing interest

The authors declare that they have no known competing financial interests or personal relationships that could have appeared to influence the work reported in this paper.

Data availability

Data will be made available on request.

Acknowledgements

The authors EPFL acknowledge the funding from SNF Consolidator Grant (BSCGI0-157705). V.P. gratefully acknowledges the funding from Piaget. Authors also thank funding from Horizon Europe Pathfinder project SOLARUP. This work was supported by the Swiss State Secretariat for Education, Research and Innovation (SERI) under contract number 22.00153. M.D. thanks funding from H2020 through SMARTCELL project (project number: 101022257). The authors also thank CIME and CMI facilities of EPFL for their technical support. H.S.M acknowledges his contract to Junta de Castilla y León.

Appendix A. Supplementary data

Supplementary data to this article can be found online at https://doi.org/10.1016/j.solmat.2023.112194.

References

[1] E.Z. Stutz, M. Zamani, D.A. Damry, L. Buswell, R. Paul, S.E. Steinvall, J.-B. Leran, J. L. Boland, M. Dimitrievska, A.F. i Morral, Showcasing the optical properties of monocrystalline zinc phosphide thin films as an earth-abundant photovoltaic absorber, Mater. Adv. 3 (2022) 1295–1303, https://doi.org/10.1039/D1MA00922B.

[2] S.E. Steinvall, N. Tappy, M. Ghasemi, R.R. Zamani, T. LaGrange, E.Z. Stutz, J.-B. Leran, M. Zamani, R. Paul, A.F. i Morral, Multiple morphologies and functionality of nanowires made from earth-abundant zinc phosphide, Nanoscale Horiz (2019), https://doi.org/10.1039/C9NH00398C.

[3] E.A. Fagen, Optical properties of Zn3P2, J. Appl. Phys. 50 (1979) 6505–6515, https://doi.org/10.1063/1.325746.

[4] J. Misiewicz, L. Bryja, K. Jezierski, J. Szatkowski, N. Mirowska, Z. Gumienny, E. Placzek-Popko, Zn3P2—a new material for optoelectronic devices, Microelectron. J. 25 (1994), https://doi.org/10.1016/0026-2692(94)90078-7 xxiii–xxviii.

[5] M. Dimitrievska, F.S. Hage, S. Escobar Steinvall, A.P. Litvinchuk, E.Z. Stutz, Q. M. Ramasse, A. Fontcuberta i Morral, The advantage of nanowire configuration in band structure determination, Adv. Funct. Mater. 41/2021, Adv. Funct. Mater. 31 (2021), 2170305, https://doi.org/10.1002/adfm.202170305.

[6] M.Y. Swinkels, A. Campo, D. Vakulov, W. Kim, L. Gagliano, S.E. Steinvall, H. Detz, M. De Luca, A. Lugstein, E. Bakkers, A. Fontcuberta i Morral, I. Zardo, Measuring the optical absorption of single nanowires, Phys. Rev. Applied. 14 (2020), 024045, https://doi.org/10.1103/PhysRevApplied.14.024045.

[7] J.M. Pawlikowski, Band structure and properties of Zn3P2— promising new infrared material, Infrared Phys. 21 (1981) 181–187, https://doi.org/10.1016/0020-0891(81)90027-0.

[8] J. Misiewicz, Inter-band transitions in Zn3P2, J. Phys. Condens. Matter 2 (1990) 2053–2072, https://doi.org/10.1088/0953-8984/2/8/012.

[9] G.M. Kimball, A.M. Müller, N.S. Lewis, H.A. Atwater, Photoluminescence-based measurements of the energy gap and diffusion length of Zn3P2, Appl. Phys. Lett. 95 (2009), 112103, https://doi.org/10.1063/1.3225151.

[10] J.M. Pawlikowski, Absorption edge of Zn3P2, Phys. Rev. B 26 (1982) 4711–4713, https://doi.org/10.1103/PhysRevB.26.4711.

[11] R. Paul, N. Humblot, S.E. Steinvall, E.Z. Stutz, S.S. Joglekar, J.-B. Leran, M. Zamani, C. Cayron, R. Logé, A.G. del Aguila, Q. Xiong, A.F. i Morral, van der Waals epitaxy of earth-abundant Zn3P2 on graphene for photovoltaics, Cryst. Growth Des. 20 (2020) 3816–3825, https://doi.org/10.1021/acs.cgd.0c00125.

[12] K.W. Mitchell, Status of new thin-film photovoltaic technologies, Annu. Rev. Mater. Sci. 12 (1982) 401–413, https://doi.org/10.1146/annurev.ms.12.080182.002153.

[13] N.C. Wyeth, A. Catalano, Spectral response measurements of minority-carrier diffusion length in Zn3P2, J. Appl. Phys. 50 (1979) 1403–1407, https://doi.org/10.1063/1.326122.

[14] J.P. Bosco, G.M. Kimball, N.S. Lewis, H.A. Atwater, Pseudomorphic growth and strain relaxation of α-Zn3P2 on GaAs(001) by molecular beam epitaxy, J. Cryst. Growth 363 (2013) 205–210, https://doi.org/10.1016/j.jcrysgro.2012.10.054.

[15] M. Bhushan, A. Catalano, Polycrystalline Zn3P2 Schottky barrier solar cells, Appl. Phys. Lett. 38 (1981) 39–41, https://doi.org/10.1063/1.92124.

[16] T. Suda, M. Kobayashi, A. Kuroyanagi, S. Kurita, Zn3P2/ITO heterojunction solar cells, Jpn. J. Appl. Phys. 21 (1982) 63, https://doi.org/10.7567/JJAPS.21S2.63.
[17] S. Demers, A. van de Walle, Intrinsic defects and dopability of zinc phosphide, Phys. Rev. B 85 (2012), 195208, https://doi.org/10.1103/PhysRevB.85.195208.
[18] K. Sierański, J. Szatkowski, A. Hajdusianek, Deep levels in low resistive Zn3P2, Physica Status Solidi (a) 214 (2017), 1600553, https://doi.org/10.1002/pssa.201600553.
[19] D. Stepanchikov, G. Chuiko, Excitons into one-axis crystals of zinc phosphide (Zn3P2), Condens. Matter Phys. 12 (2009), https://doi.org/10.5488/CMP.12.2.239.
[20] G. Lombardi, F. Maia de Oliveira, M. Daldin Teodoro, A. Chiquito, Investigation of trapping levels in p-type Zn 3 P 2 nanowires using transport and optical properties, Appl. Phys. Lett. 112 (2018), 193103, https://doi.org/10.1063/1.5026548.
[21] T. Suda, K. Kakishita, Epitaxial growth of zinc phosphide, J. Appl. Phys. 71 (1992) 3039–3041, https://doi.org/10.1063/1.350989.
[22] A. Catalano, R.B. Hall, Defect dominated conductivity in Zn3P2, J. Phys. Chem. Solid. 41 (1980) 635–640, https://doi.org/10.1016/0022-3697(80)90015-3.
[23] K. Kakishita, T. Baba, T. Suda, Zn3P2 thin films grown on glass substrates by MOCVD, Thin Solid Films 334 (1998) 25–29, https://doi.org/10.1016/S0040-6090(98)01110-9.
[24] A. Kuroyanagi, T. Suda, Single crystal growth and characterization of zinc phosphide, J. Cryst. Growth 100 (1990) 1–4, https://doi.org/10.1016/0022-0248(90)90601-G.
[25] G.M. Kimball, J.P. Bosco, A.M. Müller, S.F. Tajdar, B.S. Brunschwig, H.A. Atwater, N.S. Lewis, Passivation of Zn3P2 substrates by aqueous chemical etching and air oxidation, J. Appl. Phys. 112 (2012), 106101, https://doi.org/10.1063/1.4765030.
[26] F.-C. Wang, A. Fahrenbruch, R. Bube, Electrical properties of Zn3P2 single crystals, J. Electron. Mater. 11 (1982) 75–88, https://doi.org/10.1007/BF02654610.
[27] G.M. Kimball, N.S. Lewis, H.A. Atwater, Synthesis and Surface Chemistry of Zn3P2, 2008 33rd IEEE Photovoltaic Specialists Conference, 2008, pp. 1–6, https://doi.org/10.1109/PVSC.2008.4922747.
[28] T. Suda, K. Kakishita, H. Sato, K. Sasaki, N-type zinc phosphide grown by molecular beam epitaxy, Appl. Phys. Lett. 69 (1996) 2426–2428, https://doi.org/10.1063/1.117659.
[29] R. Katsube, H. Hayashi, A. Nagaoka, K. Yoshino, Y. Nose, Y. Shirai, Growth and characterization of indium-doped Zn3P2 bulk crystals, Jpn. J. Appl. Phys. 55 (2016), https://doi.org/10.7567/JJAP.55.041201.
[30] E.Z. Stutz, S.P. Ramanandan, M. Flór, R. Paul, M. Zamani, S.E. Steinvall, D.A. S. Salaiza, C.X. Montesinos, M. Chiara Spadaro, J.-B. Leran, A.P. Litvinchuk, J. Arbiol, A.F. i Morral, M. Dimitrievska, Stoichiometry modulates the optoelectronic functionality of zinc phosphide (Zn 3−x P 2+x), Faraday Discuss (2022), https://doi.org/10.1039/D2FD00055E.
[31] M. Zamani, E. Stutz, S. Escobar, R.R. Zamani, R. Paul, J.-B. Leran, M. Dimitrievska, A.F. i Morral, The path towards 1 μm monocrystalline Zn3P2 films on InP: substrate preparation, growth conditions and luminescence properties, J. Phys. Energy. 3 (2021), 034011, https://doi.org/10.1088/2515-7655/abf723.
[32] M. Reveil, V.C. Sorg, E.R. Cheng, T. Ezzyat, P. Clancy, M.O. Thompson, Finite element and analytical solutions for van der Pauw and four-point probe correction factors when multiple non-ideal measurement conditions coexist, Rev. Sci. Instrum. 88 (2017), 094704, https://doi.org/10.1063/1.5001830.
[33] A. Mahmood, J.-L. Wang, A review of grazing incidence small- and wide-angle X-ray scattering techniques for exploring the film morphology of organic solar cells, Solar RRL 4 (2020), 2000337, https://doi.org/10.1002/solr.202000337.
[34] J.P. Bosco, G.M. Kimball, N.S. Lewis, H.A. Atwater, Pseudomorphic growth and strain relaxation of α-Zn3P2 on GaAs(001) by molecular beam epitaxy, J. Cryst. Growth 363 (2013) 205–210, https://doi.org/10.1016/j.jcrysgro.2012.10.054.
[35] M. zubair Ansari, N. Khare, Thermally activated band conduction and variable range hopping conduction in Cu2ZnSnS4 thin films, J. Appl. Phys. 117 (2015), 025706, https://doi.org/10.1063/1.4905673.
[36] R. Kumar, N. Khare, Temperature dependence of conduction mechanism of ZnO and Co-doped ZnO thin films, Thin Solid Films 516 (2008) 1302–1307, https://doi.org/10.1016/j.tsf.2007.06.121.
[37] N. Mirowska, J. Misiewicz, Defect-related transitions in Zn3P2 studied by means of photovoltaic effect spectroscopy, Semicond. Sci. Technol. 7 (1992) 1332–1336, https://doi.org/10.1088/0268-1242/7/11/007.
[38] M. Grundmann, The Physics of Semiconductors: an Introduction Including Nanophysics and Applications, Springer International Publishing, Cham, 2016, https://doi.org/10.1007/978-3-319-23880-7.
[39] M. Rudra, H.S. Tripathi, A. Dutta, T.P. Sinha, Existence of nearest-neighbor and variable range hopping in Pr2ZnMnO6 oxygen-intercalated pseudocapacitor electrode, Mater. Chem. Phys. 258 (2021), 123907, https://doi.org/10.1016/j.matchemphys.2020.123907.
[40] H. Matsuura, A. Takeshita, T. Imamura, K. Takano, K. Okuda, A. Hidaka, S. Ji, K. Eto, K. Kojima, T. Kato, S. Yoshida, H. Okumura, Transition of conduction mechanism from band to variable-range hopping conduction due to Al doping in heavily Al-doped 4H-SiC epilayers, Jpn. J. Appl. Phys. 58 (2019), 098004, https://doi.org/10.7567/1347-4065/ab3c2c.
[41] B. Bhattacharyya, A. Sharma, B. Sinha, K. Shah, S. Jejurikar, T.D. Senguttuvan, S. Husale, Evidence of robust 2D transport and Efros-Shklovskii variable range hopping in disordered topological insulator (Bi2Se3) nanowires, Sci. Rep. 7 (2017), https://doi.org/10.1038/s41598-017-08018-6.
[42] A. Masarrat, A. Bhogra, R. Meena, R. Urkude, A. Niazi, A. Kandasami, Enhancement of the thermoelectric properties and transition of conduction mechanism from nearest neighbor to variable range hopping of Ni-doped CoSb3, J. Electron. Mater. 51 (2022) 3350–3358, https://doi.org/10.1007/s11664-022-09547-1.
[43] G. Cucinotta, L. Poggini, N. Giaconi, A. Cini, M. Gonidec, M. Atzori, E. Berretti, A. Lavacchi, M. Fittipaldi, A.I. Chumakov, R. Rüffer, P. Rosa, M. Mannini, Space charge-limited current transport mechanism in crossbar junction embedding molecular spin crossovers, ACS Appl. Mater. Interfaces 12 (2020) 31696–31705, https://doi.org/10.1021/acsami.0c07445.
[44] X.-G. Zhang, S.T. Pantelides, Theory of space charge limited currents, Phys. Rev. Lett. 108 (2012), 266602, https://doi.org/10.1103/PhysRevLett.108.266602.
[45] V.M. Le Corre, E.A. Duijnstee, O. El Tambouli, J.M. Ball, H.J. Snaith, J. Lim, L.J. A. Koster, Revealing charge carrier mobility and defect densities in metal halide perovskites via space-charge-limited current measurements, ACS Energy Lett. 6 (2021) 1087–1094, https://doi.org/10.1021/acsenergylett.0c02599.
[46] M. Sajedi Alvar, P.W.M. Blom, G.-J.A.H. Wetzelaer, Space-charge-limited electron and hole currents in hybrid organic-inorganic perovskites, Nat. Commun. 11 (2020) 1–9, https://doi.org/10.1038/s41467-020-17868-0.
[47] E.A. Duijnstee, J.M. Ball, V.M. Le Corre, L.J.A. Koster, H.J. Snaith, J. Lim, Toward understanding space-charge limited current measurements on metal halide perovskites, ACS Energy Lett. 5 (2020) 376–384, https://doi.org/10.1021/acsenergylett.9b02720.
[48] M. Taukeer Khan, A. Almohammedi, S. Kazim, S. Ahmad, Electrical methods to elucidate charge transport in hybrid perovskites thin films and devices, Chem. Rec. 20 (2020) 452–465, https://doi.org/10.1002/tcr.201900055.
[49] M. Soylu, B. Abay, Analysing space charge-limited conduction in Au/n-InP Schottky diodes, Phys. E Low-dimens. Syst. Nanostruct. 43 (2010) 534–538, https://doi.org/10.1016/j.physe.2010.09.012.
[50] X.M. Shen, D.G. Zhao, Z.S. Liu, Z.F. Hu, H. Yang, J.W. Liang, Space-charge-limited currents in GaN Schottky diodes, Solid State Electron. 49 (2005) 847–852, https://doi.org/10.1016/j.sse.2005.02.003.
[51] T. Suda, R.H. Bube, Deep levels in zinc phosphide, Appl. Phys. Lett. 45 (1984) 775–777, https://doi.org/10.1063/1.95400.
[52] M.A. Lampert, Simplified theory of space-charge-limited currents in an insulator with traps, Phys. Rev. 103 (1956) 1648–1656, https://doi.org/10.1103/PhysRev.103.1648.
[53] G.K. Gupta, V.R. Reddy, A. Dixit, Impact of excess and disordered Sn sites on Cu2ZnSnS4 absorber material and device performance: a 119Sn Mössbauer study, Mater. Chem. Phys. 225 (2019) 410–416, https://doi.org/10.1016/j.matchemphys.2018.12.078.
[54] H. Sheoran, V. Kumar, R. Singh, A comprehensive review on recent developments in ohmic and Schottky contacts on Ga2O3 for device applications, ACS Appl. Electron. Mater. 4 (2022) 2589–2628, https://doi.org/10.1021/acsaelm.2c00101.
[55] W.-J. Yin, Y. Yan, The electronic properties of point defects in earth-abundant photovoltaic material Zn3P2: a hybrid functional method study, J. Appl. Phys. 113 (2013), 013708, https://doi.org/10.1063/1.4772708.
[56] V.S. Babu, P.R. Vaya, J. Sobhanadri, Doping of Zn_3P_2 thin films during growth using the hot wall deposition technique and some properties of the grown films, Semicond. Sci. Technol. 4 (1989) 521–525, https://doi.org/10.1088/0268-1242/4/7/004.
[57] Faa-Ching Wang, R.H. Bube, R.S. Feigelson, R.K. Route, Single crystal growth of Zn3P2, J. Cryst. Growth 55 (1981) 268–272, https://doi.org/10.1016/0022-0248(81)90024-5.